

Monochromatic Propagation-Based Phase-Contrast Microscale Computed-Tomography System with a Rotating-Anode Source

L. Brombal,^{1,*} G. Kallon,² J. Jiang,² S. Savvidis,² P. De Coppi,^{3,4} L. Urbani,³ E.J. Forty,⁵ R.C. Chambers,⁵ R. Longo,¹ A. Olivo,² and M. Endrizzi²

¹*Department of Physics, University of Trieste, Trieste 34217, Italy and Istituto Nazionale di Fisica Nucleare, Division of Trieste, Trieste 34217, Italy*

²*Department of Medical Physics and Biomedical Engineering, University College London, London WC1E 6BT, United Kingdom*

³*Department of Surgery, University College London Institute of Child Health, London WC1N 1EH, United Kingdom*

⁴*Great Ormond Street Hospital for Children, London WC1N 3JH, United Kingdom*

⁵*Centre for Inflammation and Tissue Repair, UCL Respiratory, Rayne Building, University College London, London WC1E 6JF, United Kingdom*

(Received 4 October 2018; revised manuscript received 10 December 2018; published 4 March 2019)

We present an experimental setup for monochromatic propagation-based x-ray phase-contrast imaging based on a conventional rotating-copper-anode source, capable of an integrated flux up to 10^8 photons/s at 8 keV. In our study, the system is characterized in terms of spatial coherence, resolution, contrast sensitivity, and stability. Its quantitativeness is demonstrated by comparing theoretical predictions with experimental data on simple wire phantoms both in planar and computerized-tomography-scan geometries. Application to two biological samples of medical interest shows the potential for bioimaging on the millimeter scale with spatial resolution of the order of $10\ \mu\text{m}$ and contrast resolution below 1%. All the scans are performed within laboratory-compatible exposure times, from 10 min to a few hours, and trade-offs between scan time and image quality are discussed.

DOI: 10.1103/PhysRevApplied.11.034004

I. INTRODUCTION

X-ray imaging is arguably the most used technique for nondestructive investigation of internal features in bulk samples, covering a vast range of applications from industrial inspection to clinical radiology. Conventional radiography relies on the contrast arising from the different absorption properties of details within a sample. A key limitation of conventional x-ray approaches is that, when dealing with low-Z materials (e.g., soft tissues and plastics), absorption differences can become so small that the sample features are no longer distinguishable. In this context, x-ray phase-contrast imaging (XPCI) offers significant advantages, because it is sensitive to the refractive properties of the sample. In fact, over a wide range of energies from few to hundreds of kilo electron

volt, the decrement (δ) of the complex refractive index (n), responsible for refraction, is 2 or 3 orders of magnitude higher than the imaginary term (β) responsible for absorption.

Over the past two decades, several techniques have been developed to transform phase effects into intensity modulation on the detector: propagation-based, analyzer-based, edge-illumination, and interferometric techniques are currently in use with synchrotron and, in some cases, conventional sources [1–4]. Among these approaches, propagation-based imaging (PBI) is the simplest to implement, as it only requires some propagation distance between the sample and the detector, without the need for optical elements or multiexposures [5]. However, with respect to other techniques, PBI has more stringent requirements on the spatial coherence of the x-ray source and, especially at small magnifications, on the spatial resolution of the detector. For this reason, most of its applications have been so far limited either to synchrotron-radiation facilities or to low-power microfocal sources [2,6–9]. In this context, the development of compact and partially coherent high-flux x-ray sources is an active area of research [10,11].

*luca.brombal@ts.infn.it

Published by the American Physical Society under the terms of the [Creative Commons Attribution 4.0 International license](#). Further distribution of this work must maintain attribution to the author(s) and the published article's title, journal citation, and DOI.

Several laboratory x-ray sources, based either on liquid-metal or rotating targets, are capable of producing sufficient flux and spatial coherence to be used for phase-contrast imaging purposes, the main advantages being robustness, availability, compactness, and low costs [12–15]. Moreover, monochromator crystals selecting the characteristic x-ray lines can be coupled to the source, thus producing quasimonochromatic spectra. It is noteworthy that, albeit not being essential for XPCI, the use of narrow monochromatic radiation is advantageous, as it allows a straightforward quantitative analysis to be performed and avoids beam-hardening effects.

From the theoretical point of view, due to the limited degree of spatial coherence and detector resolution, PBI can be described in terms of the ray-optical approximation in most practical applications [16,17]. Let us consider a monochromatic and parallel x-ray beam of wavelength λ , propagating along the z axis, impinging on a refractive object located in the x - y plane. The phase shift Φ imparted to the beam is given by [17]

$$\Phi(x, y; \lambda) = -\frac{2\pi}{\lambda} \int_{\text{object}} \delta(x, y, z; \lambda) dz, \quad (1)$$

where the integral extends over the entire object thickness (i.e., the projection approximation). The object-induced phase shift will result in a slight deviation (i.e., refraction) of the incident beam which, in the paraxial approximation, can be described by the refraction angle:

$$\alpha(x, y; \lambda) \simeq \frac{\lambda}{2\pi} |\nabla_{xy} \Phi(x, y; \lambda)|, \quad (2)$$

where ∇_{xy} is the gradient operator in the x - y object plane. In the simple case of a homogeneous cylinder of radius r oriented along the y direction (e.g., a wire), the integral in Eq. (1) can be solved and the refraction angle is expressed as follows:

$$\alpha(x) \simeq \frac{2\delta x}{\sqrt{r^2 - x^2}}. \quad (3)$$

Considering the propagation process of the refracted photons to the detector plane and also taking into account the more general geometry of a diverging beam (i.e., a point-like source at a finite distance), it can be demonstrated that the intensity recorded at a propagation distance z' is [17]

$$I_{\text{ref}}(x, y; M; \lambda) \simeq I_0 \left[1 - \frac{z' \lambda}{2\pi M} \nabla_{xy}^2 \Phi(x, y; \lambda) \right], \quad (4)$$

where I_0 is the intensity that would have been observed without the object and M is the magnification factor. In order to also include the absorption properties of the sample, the refraction signal described by the previous

equation must be modulated by the object transmission function:

$$I(x, y; M; \lambda) \simeq I_0 \left[1 - \frac{z' \lambda}{2\pi M} \nabla_{xy}^2 \Phi(x, y; \lambda) \right] T(x, y; \lambda), \quad (5)$$

where the term T describes the transmission according to the Beer-Lambert law [17]. From Eq. (5), it is clear how both contrast mechanisms, absorption and phase, come into play: the Laplacian of the phase shift will be significantly different from zero across sharp interfaces, producing a strong phase-contrast signal (i.e., an edge-enhancement effect) conversely, within smooth regions of the sample, the Laplacian vanishes, and only the absorption contrast will be observed. So far, the ideal case of a pointlike source and an infinitely sharp detector response has been considered. In an actual experiment, both the detector-response unsharpness and the source size must be taken into account. In fact, along with the propagation distance, the overall signal broadening described by the system response point spread function (PSF), \mathcal{F}_{sys} , determines whether phase effects can be observed. The response function can be written as follows:

$$\mathcal{F}_{\text{sys}}(x, y; M; \lambda) = \mathcal{F}_{\text{det}}(Mx, My; \lambda) * \mathcal{F}_{\text{src}}\left(\frac{M}{M-1}x, \frac{M}{M-1}y; \lambda\right), \quad (6)$$

where $*$ indicates convolution, \mathcal{F}_{det} is the detector response to a Dirac-delta-like input and \mathcal{F}_{src} is the spatially varying intensity distribution of the source (i.e., a measure of the spatial coherence at a given magnification) [18–20]. The detected signal will be given by the convolution between the ideal intensity and the system response:

$$I'(x, y; M; \lambda) = I(x, y; M; \lambda) * \mathcal{F}_{\text{sys}}(x, y; M; \lambda). \quad (7)$$

It is clear that having a large source size and/or a broad detector response would result in a smearing of the edge-enhancement effect, thus significantly reducing the phase contrast.

Assuming either the weak-absorption or homogeneity conditions, the phase shift induced by the object can be retrieved from a single PBI image, meaning that Eq. (5) can be inverted [21,22]. Among the several phase-retrieval techniques available, Paganin's approach, based on the homogeneous transport-of-intensity equation, is arguably the most used and it is assumed that the absorption and refraction properties are proportional throughout the sample (i.e., $\delta/\beta = \text{const}$) [21]. From a signal-processing perspective, phase retrieval can be described as a low-pass filter, which, in the spatial-frequency domain (u, v), can

be written as follows [22,23]:

$$H(u, v) = \left[1 + \pi \lambda z' \frac{\delta}{\beta} (u^2 + v^2) \right]^{-1}, \quad (8)$$

where, once the propagation geometry and the beam energy have been fixed, δ/β is the only tunable parameter of the filter. It has been demonstrated that the application of the filter, when used in combination with PBI, results in an image with a major noise reduction without a significant reduction in spatial resolution [24–27]. In addition, even if the presence of a single homogeneous material is assumed in its derivation, Paganin's phase retrieval can be adapted to strongly heterogeneous samples via multimaterial approaches [28,29].

This work makes use of the aforementioned theoretical background and reports on a microscale computed-tomography (μ -CT) monochromatic PBI setup based on a high-power rotating-anode x-ray generator suitable for biological samples on the millimeter scale. In the following, the system is characterized in terms of spatial resolution, coherence, quantitiveness, stability, and contrast sensitivity and considerations are given on trade-offs between the scan time and the image quality. Planar and tomographic images of custom-built wire phantoms are acquired and compared with theoretical predictions. In addition, we show two applications to biological samples, demonstrating the feasibility of monochromatic PBI μ -CT with laboratory-compatible exposure times from tens of minutes to hours.

II. MATERIALS AND METHODS

A. Imaging setup

A schematic overview of the experimental setup is given in Fig. 1. X rays are produced by a Rigaku Multi-Max 9 rotating-anode source, featuring a copper anode and operated at 46 kV(peak) and 26 mA, corresponding to a power of 1.2 kW. The source is coupled to a double-bent multilayer VariMax Cu-HF monochromator, providing an energy resolution of about 1% at 8 keV (Cu $K\alpha$ emission lines) and focusing the beam to a 210 μ m

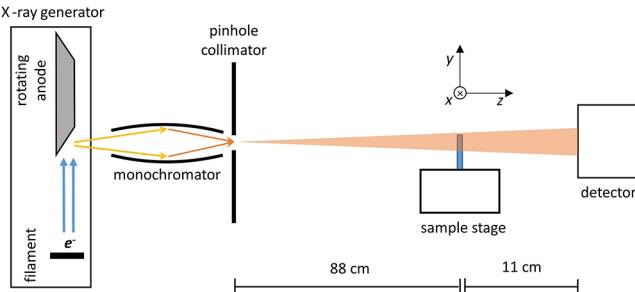


FIG. 1. A schematic overview of the experimental setup.

focal spot [30,31]. The source dimension is defined by a gold-plated pinhole collimator with a diameter of 75 μ m, located at the focus position of the monochromator. This arrangement (i.e., the monochromator and collimator) results in an integrated flux of about 10^8 photons/s and a divergence of 5 mrad. The sample is positioned at 88 cm from the source, while the propagation distance is set to 11 cm, corresponding to a magnification of $M = 1.13$. At this distance, the field of view is diamond shaped, with dimensions of about 5×5 mm². The sample alignment and rotation are performed through a piezometric motor stack with 5 degrees of freedom and submicrometric precision. The imaging detector is a charge-coupled device (CCD) camera featuring a 4.54 μ m pixel size, coupled through a fiber-optic plate to a Gadox scintillator (Photonic Science). Both the detector PSF and the source intensity distribution are measured with the slanted-edge technique by using a 50 μ m thick lead blade, the unsharpness and finite-thickness effects of which can be neglected given the system's energy and spatial resolution [32].

B. Acquisition parameters

The planar acquisition is performed with an overall exposure time of 100 s. The long-exposure CT scans are acquired over 1440 projections, with exposure times of 10 s per projection for the wire phantom and 6 s per projection for the biological samples, corresponding to total exposure times of 4 and 2.4 h, respectively. In the fast scans, the total exposure time is reduced by a factor of 20 in the case of the wire phantom, by acquiring 720 projections with an exposure of 1 s, and by a factor of 10 in the case of the biological sample, by acquiring 720 projections with an exposure of 1.2 s, resulting in total exposures of 12 and 14 mins, respectively. During the long scans, a flat-field image (i.e., without the sample in place) is acquired every 30 projections to monitor the beam intensity.

C. Phantoms and samples

Two wire phantoms are built for planar and CT acquisition geometries. They both consist of three different high-purity plastic rods made of polybutylene terephthalate (PBT), polyethylene terephthalate (PET), and nylon. The absorption and refraction coefficients used for the theoretical calculations are listed in a publicly available database [33] and are reported in Table I.

The scans of two biological samples are reported in this work. The first sample is an oesophageal acellular matrix (ACM), derived from a piglet, provided by the Institute of Child Health (ICH). The ACM is derived via an established decellularization technique called detergent enzymatic treatment (DET) [34,35]. Following the DET, the sample is critical-point dried using CO₂. The sample has an approximate size of $5 \times 5 \times 3$ mm³. The second sample is a lobe (dimensions approximately $3 \times 5 \times$

TABLE I. The physical properties of the wires used for the phantoms.

	$\delta \times 10^{-6}$	$\beta \times 10^{-9}$	δ/β	Density (g/cm ³)	Diameter (μm)
PBT	4.45	9.79	454	1.31	180
PET	4.70	11.1	423	1.40	400
Nylon	3.99	7.25	550	1.13	160

3 mm³) of a dehydrated fibrotic murine lung, generated from a bleomycin-induced lung fibrosis model (sample collected 28 days post-bleomycin, 25 IU) as described previously [36]. For CT acquisitions, all the samples are positioned within a thin plastic cylinder fixed on the rotation stage.

D. Data processing and reconstruction

The planar data are processed by a conventional dark-current subtraction and flat-field normalization, whereas for CT scans the projections are normalized using a dynamic flat-field approach based on principal-component analysis of the flat images to compensate for beam-intensity variations over long exposures [37]. The normalized projections are (optionally) phase retrieved and reconstructed via a graphics-processing-unit- (GPU-)based filtered back projection with a standard Shepp-Logan filter [38]. The reconstruction is performed in a parallel beam geometry since, considering the small sample sizes and setup geometry, the beam divergence within the sample is smaller than the system spatial resolution and thus does not require the use of a cone-beam reconstruction.

III. RESULTS

A. Simulation and system characterization

The overall spatial resolution of the system is the key parameter in determining whether or not phase effects can be observed. In Fig. 2, the measured detector PSF (left), the source distribution (center), and their convolution (right)

are reported as functions of the spatial coordinate at the sample position according to Eq. (6). The experimental-system PSF has been fitted with a linear combination of a Lorentzian and a Gaussian function. The blurring due to the detector response is of 12 μm full width at half maximum (FWHM), while the source size projected at the sample position is of about 10 μm , resulting in an overall resolution of about 14 μm FWHM.

Given the system PSF, the intensity profile given by a wire of known composition can be theoretically calculated according to Eqs. (2)–(7). In the left panel of Fig. 3, the refraction (blue line), transmission (red line), and total (black line) intensity profiles calculated according to Eq. (5) are reported. Despite the smearing due to the convolution with the system PSF (central panel), the expected signal (right panel) still shows edge-enhancement contrast, indicating that the system's spatial coherence and spatial resolution are sufficient to detect phase effects.

B. Planar imaging of the wire phantom

The first test of the system quantitativeness is performed by imaging a planar phantom consisting of three vertically oriented wires made of PBT, PET, and nylon, plus one horizontal PBT wire [Fig. 4(a)]. For each of the vertical wires, a line intensity profile is compared against their respective theoretical profiles, accounting for the nominal values of density, absorption, and refraction of each material [Figs. 4(b)–4(d)]. The overall agreement between the theory and the experimental data is remarkable considering both the phase and absorption contrast,

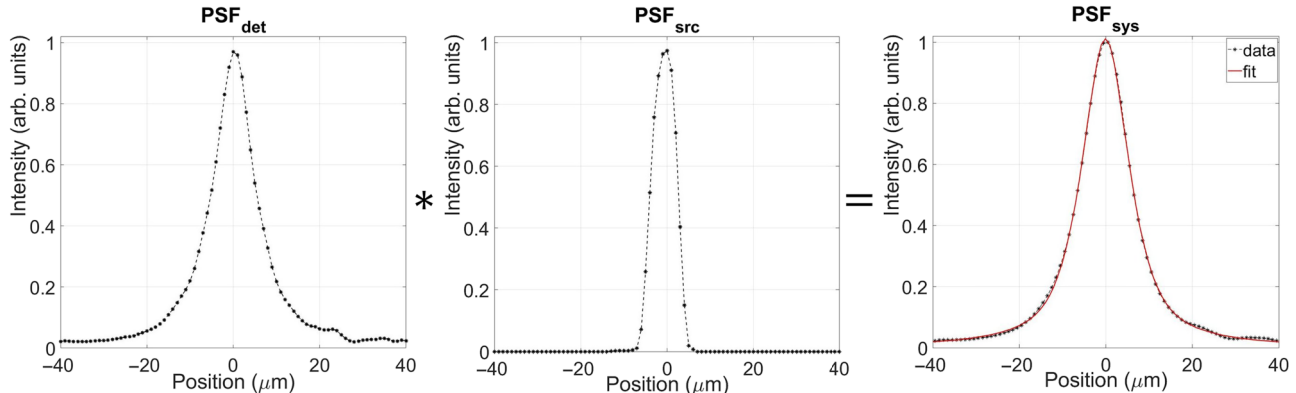


FIG. 2. The detector (left), source (center), and system (right) PSFs projected at the sample position. The system PSF has been fitted (red solid line) with a linear combination of a Lorentzian and a Gaussian function.

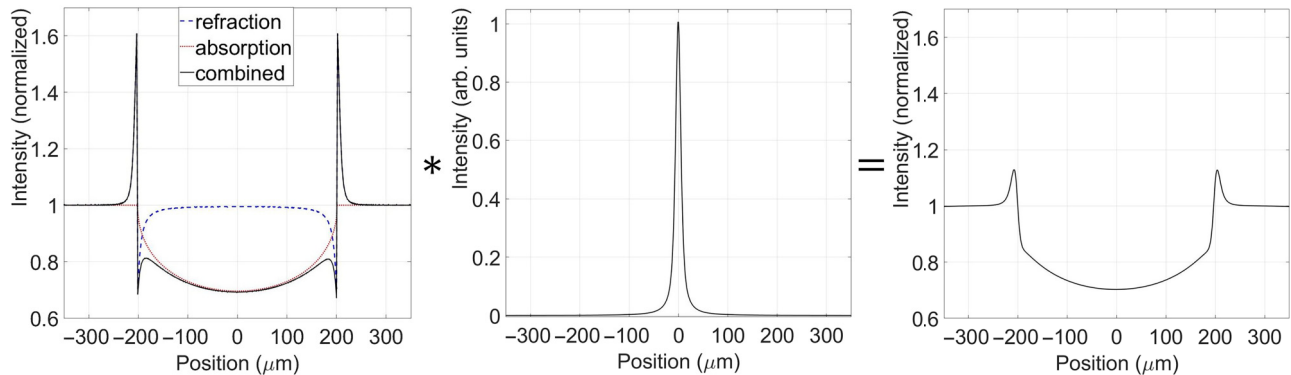


FIG. 3. The theoretical refraction, absorption, and total profiles produced by a homogeneous wire (left), the system PSF (center), and their convolution (right).

the largest discrepancy being a slight underestimate (< 5%) of the PET absorption. Moreover, by comparing profiles extracted from both the horizontal and vertical PBT wires [Fig. 4(b)], the same phase sensitivity is achieved in both directions due to the circular symmetry of the source.

C. CT imaging of the wire phantom

The same wires are used to assess the system performance in CT acquisitions. The sample is scanned with an exposure time of 4 h. In Fig. 5(a), a tomographic slice is shown: due to the beam monochromaticity, the reconstruction is inherently quantitative and thus (far from the refraction fringes) the gray level represents the linear attenuation coefficient. To obtain the theoretical profiles for the

CT case, a sinogram composed of a set of identical line profiles is created for each wire and then reconstructed following the same work flow used for the experimental data. As for the planar image, good agreement is observed when comparing the theoretical and experimental profiles across the wires for both the phase and absorption signals, except for a small discrepancy (< 10%) in the absorption coefficient of PET [Figs. 5(b)–(d)]. The fact that the refraction fringes are well matched by the theoretical predictions for a scan acquired over several hours provides an indirect assessment of the system's stability and the piezometric motors' reproducibility: vibrations or spatial drifts of the source, sample, or detector, or slight inaccuracies in the sample repositioning after acquisition of the periodic flat-field images, would result in a broader effective PSF, thus smearing out the fringes. Furthermore, by defining

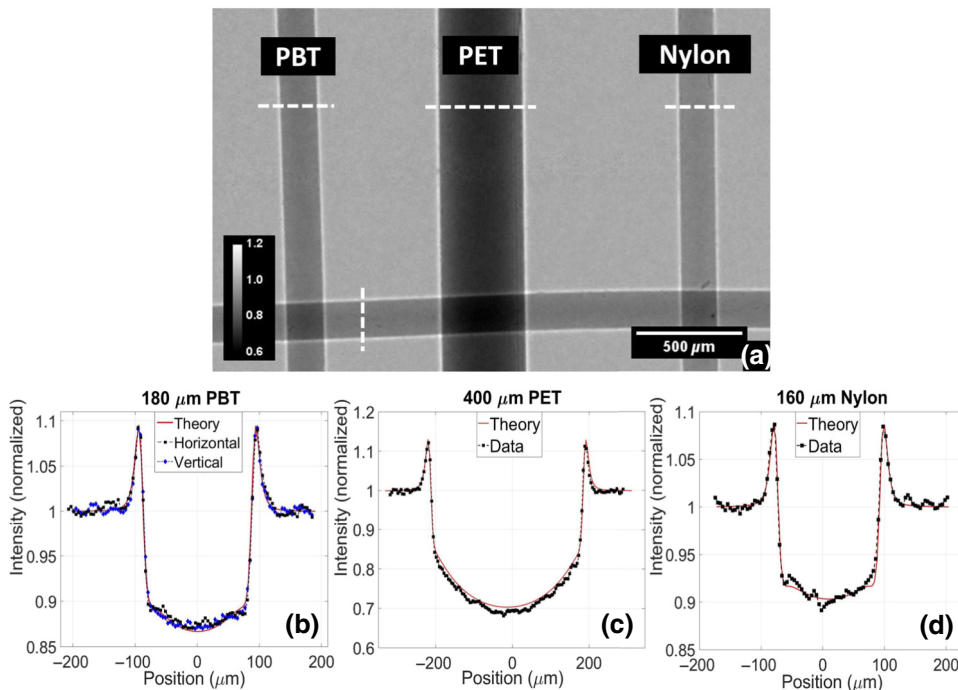


FIG. 4. An image of the planar wire phantom (a) and plots of the intensity profiles (b)–(d) along the white dashed lines. The image results from dark-current subtraction and flat-field normalization.

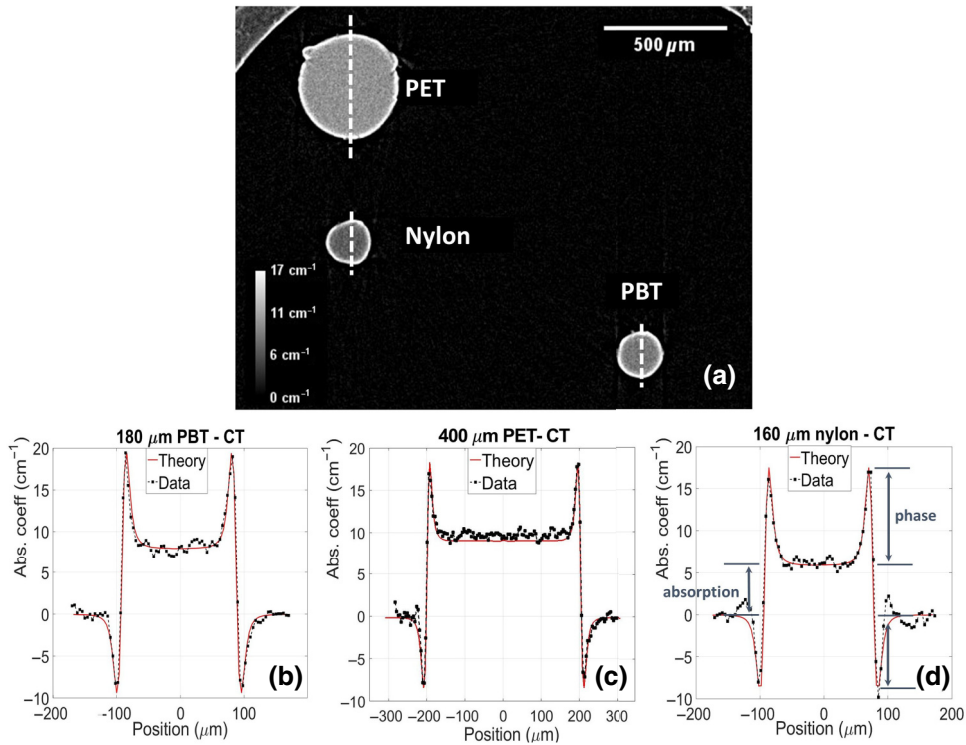


FIG. 5. A reconstructed slice of the wire phantoms (a) and plots of the intensity profiles (b)–(d) along the white dashed lines. The structure visible in the top left- and right-hand corners of (a) is part of the cylinder that was used to keep the phantom in place.

the refraction signal as the sum of the overshoots of the dark and bright fringes (see Fig. 5(d)), this is in all cases between 1.5 and 3 times higher than the absorption signal.

As discussed in the previous section, the CT projections are processed by applying Paganin's single-shot phase-retrieval algorithm. In order to adequately choose the filter parameter, it is common practice to tweak δ/β until the refraction fringes disappear without introducing an excessive smoothing. We demonstrate this practice by showing different profiles taken across the PBT wire in Fig. 6. Each profile is reconstructed using a δ/β value in the range of 250–550: due to the beam monochromaticity, it is found that the optimal δ/β is 450, which matches its nominal value well (see Table I).

In Fig. 7(a), the phase-retrieved reconstruction of the wire phantom is shown. Here, $\delta/\beta = 450$ is used, as it is an intermediate value among the three different plastics. As expected, the refraction fringes are no longer visible, while the noise has been significantly suppressed. This can be clearly appreciated in the gray-level histograms in Figs. 7(c) and 7(d), which are obtained by selecting circular regions of interest (ROIs) at the center of each wire for both the images with and without phase retrieval: after phase retrieval, the three materials can be easily separated based on the gray values of each voxel. The ROIs are selected far from edges where the gray-level distribution is flat and have equal areas to provide histograms with equal statistics. Given the high contrast sensitivity achieved with phase retrieval, the same sample has been scanned while reducing the exposure time by a

factor of 20 (from 4 h to 12 min), as shown in Fig. 7(b). Even though a broadening of the distributions due to the reduced statistics is observed, the histogram in Fig. 7(e) shows that the materials are still clearly distinguishable. In quantitative terms, we observe that the central values of the gray-level distributions are separated, respectively, by approximately 25 standard deviations for the long-exposure scans and approximately 10 for the short-exposure scans. This clear separation, between materials of similar attenuation properties, is advantageous in all

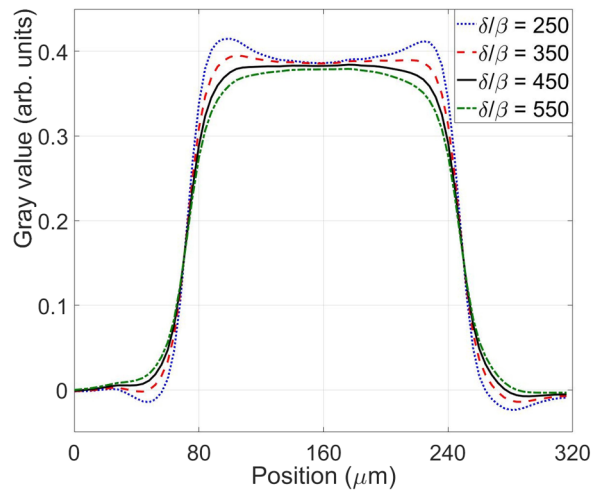


FIG. 6. Intensity profiles across the PBT wire at different values of δ/β .

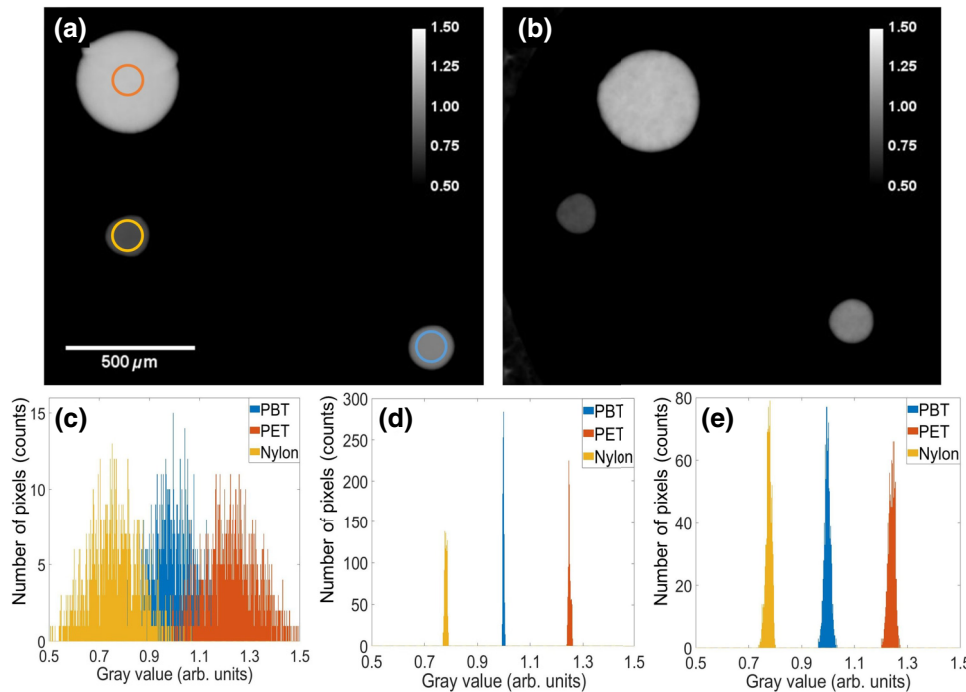


FIG. 7. An image of the wire phantom after phase retrieval for the 4-h long exposure (a) and the 12 min long exposure (b). In (a), the ROIs used for the histograms are reported. The gray-level histograms are relative to the wires that are phantom reconstructed without [(c), see also Fig. 5] and with phase retrieval for the long (d) and short (e) exposures.

those applications involving subsequent data-processing steps such as segmentation.

The quantitative results extracted from tomographic images are summarized in Table II. For all materials, the measured attenuation coefficient is compatible, within the noise fluctuations, with the theoretical values; the maximum discrepancy in terms of mean value is observed for PET wire and it is smaller than 10%. This result is compatible with the findings of the planar image, where PET has been found to be more absorbing than its nominal value. To estimate the effects of phase retrieval, the contrast (C) with respect to the least absorbing material, i.e., nylon, has been measured both before and after the application of the retrieval algorithm. As expected, no significant differences in the detected contrast are observed, indicating that the image retains its quantitativeness. On the contrary, a major improvement in the contrast sensitivity (i.e., the associated uncertainty), going from about 20% to values smaller than 1%, is found. Also, when the short-exposure acquisition is considered, the contrast sensitivity is still around 2%, clearly sufficient for material differentiation, while no contrast variation is observed.

D. Biological samples

Two biological samples are scanned. In Figs. 8(a) and 8(b), a CT scan of an oesophageal acellular matrix derived from a piglet is shown before and after applying phase retrieval ($\delta/\beta = 100$), respectively, with an exposure time of 2.4 h. The same sample has been scanned 10 times faster, corresponding to an exposure time of 14 min [Fig. 8(c)]. Focusing on the detail shown in Figs. 8(d)–8(f), it is clear that the high noise in the non-phase-retrieved image possibly hampers the ability to differentiate soft tissues while, when phase retrieval is applied, the contrast sensitivity is sufficient to distinguish the four layers composing the esophageal wall, namely mucosa, submucosa, muscularis propria, and adventitia. Remarkably, despite a higher noise level, the tissue layers are also distinguishable in the short-exposure scan.

Figures 9(a) and 9(b) show a phase-retrieved ($\delta/\beta = 50$) transaxial slice and a three-dimensional (3D) rendering of a fibrotic mouse lung sample, respectively. Dense fibrotic tissue can be distinguished in the subpleural peripheral and bronchovascular regions in the transaxial slice, with

TABLE II. The quantitative results obtained from the CT reconstructions. “ $C(\text{NPR})$, $C(\text{PR})$, and $C(\text{SPR})$ ” refer to the contrast of long-exposure non-phase-retrieved, phase-retrieved, and short-exposure phase-retrieved acquisitions, respectively. Uncertainties are computed by following standard error-propagation rules.

	$\mu_{\text{th}}(\text{cm}^{-1})$	$\mu_{\text{exp}}(\text{cm}^{-1})$	Rel. error (%)	$C(\text{NPR})$ (%)	$C(\text{PR})$ (%)	$C(\text{SPR})$ (%)
PBT	7.98	7.8 ± 0.8	-1.8	30 ± 18	27.9 ± 0.7	28.5 ± 2.0
PET	9.01	9.8 ± 0.8	8.7	62 ± 20	59.9 ± 0.8	59.9 ± 2.2
Nylon	5.91	6.0 ± 0.8	2.0

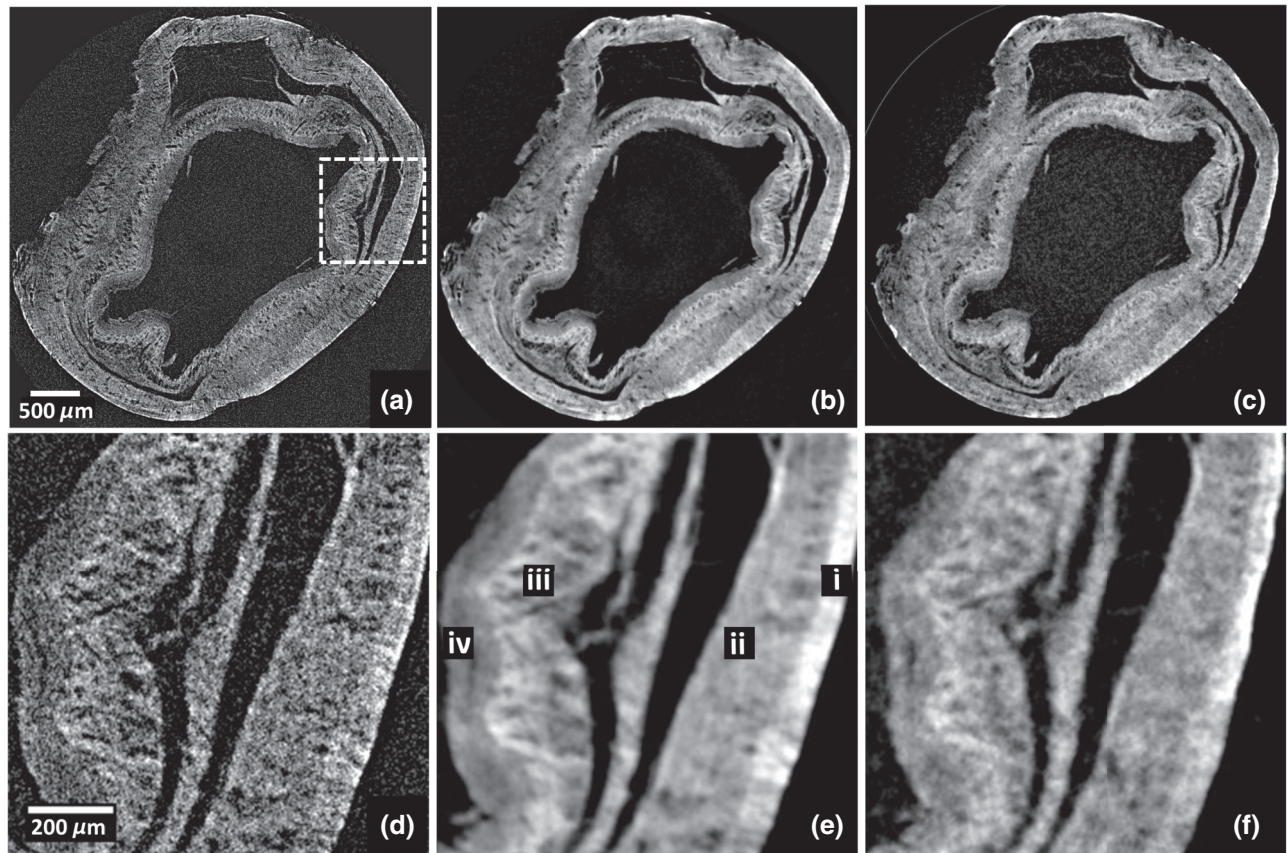


FIG. 8. A decellularized piglet-esophagus scan with long exposure without (a),(d) and with (b),(e) phase retrieval, and with short exposure with phase retrieval (c),(f). The dashed square in (a) represents the detail that is enlarged in the lower panels. The labels in (e) identify, from right to left, adventitia (i), muscularis propria (ii), submucosa (iii) and mucosa (iv).

bronchi and bronchioles a prominent feature in the 3D rendering. Quantification of changes in parenchymal density, as seen in fibrosis, or measurement of airway or vascular remodeling, represent potential preclinical applications of this imaging technique.

IV. DISCUSSION AND CONCLUSIONS

This study shows that quantitative phase imaging based on a high-power rotating-copper-anode source is feasible,

with laboratory-compatible scan times from tens of minutes to a few hours. Specifically, the setup is appealing for light materials, such as plastics or soft tissues, with dimensions on the millimeter scale, requiring high contrast sensitivity and spatial resolution of the order of $10 \mu\text{m}$. The x-ray source, coupled with a monochromator selecting the $\text{Cu } K\alpha$ characteristic line (8 keV) and a gold-plated pinhole collimator, has an integrated flux of 10^8 photons/s and a divergence of 5 mrad. The system is characterized in terms of spatial coherence and detector spatial resolution, resulting in an overall PSF at the sample position of $14 \mu\text{m}$ FWHM. This value represents an optimal trade-off between the spatial coherence and the x-ray flux, since the source size projected at the sample position is comparable to the detector PSF. Profiles of homogeneous plastic wires are simulated, starting from theoretical calculations for planar and CT acquisitions and the quantitativeness of the system is demonstrated by matching experimental and theoretical profiles. Overall, good agreement is found for both the phase and absorption signals, the maximum difference being $< 5\%$ in planar and $< 10\%$ in CT. The setup stability over several hours is proven by the remarkable agreement between the predicted and expected intensities

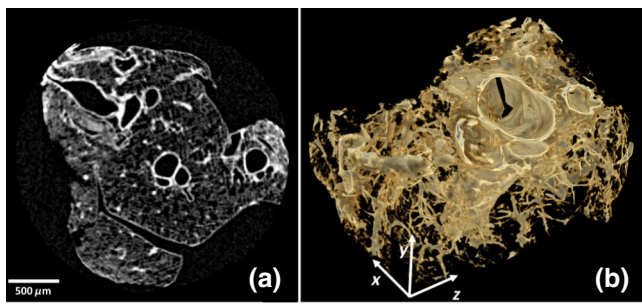


FIG. 9. A transaxial slice (a) and 3D rendering (b) of the fibrotic mouse lung sample.

of the refraction fringes, which would have been smeared out in the case of non-negligible vibrations or drifts occurring during the scan. Furthermore, with reference to the wire phantom, the refraction signal in the CT scan is proven to be 2–3 times higher than absorption. The effects of the phase-retrieval algorithm on the contrast sensitivity are examined, showing a 20-fold improvement in contrast sensitivity (from approximately 20% to $\lesssim 1\%$). The possibility of a significant reduction in exposure time is investigated, showing that, when going from 4 h to 12 min, the contrast resolution remains around 2%, still providing a fine resolving power between different soft materials. In addition, the system is tested on two biological samples of medical interest for potential preclinical applications (e.g., digital histology and some aspects of regenerative medicine, such as tissue-scaffold interactions), with overall dimensions on the millimeter scale. In more detail, the scan of the piglet-esophagus sample shows the capability of distinguishing the layered structure of the esophageal wall both with long (2.4 h) and short (14 min) exposure times, while the volume reconstruction of the mouse lung sample highlights both the spatial resolution and the 3D capabilities of the system.

As a general remark, it is worth noting that, in addition to the configuration reported in this study, the setup is inherently flexible, as it allows adjustment of the spatial coherence, by replacing the pinhole collimator defining the source size, and the magnification. Moreover, by inserting a vacuum pipe to prevent air attenuation, the field of view can, in principle, be enlarged at a constant fluence rate. In fact, keeping the spatial coherence constant, the linear source size d (i.e., the collimator diameter) can be scaled with the source-to-detector distance R , thus compensating the fluence-rate reduction due to the larger source-to-detector distance by the larger dimension of the source:

$$\text{fluence rate (photons/mm}^2/\text{s}) \propto \frac{d^2}{R^2} \propto \frac{R^2}{R^2} = \text{constant.} \quad (9)$$

This is possible since the focus created by the bent-multilayer monochromator is significantly larger (approximately 210 μm) than the pinhole collimator itself (75 μm). Moreover, when using other XPCI techniques that are less demanding in terms of spatial coherence (e.g., edge illumination), the same setup can be used with larger collimators, potentially delivering a 10 times higher flux.

ACKNOWLEDGMENTS

G.K. was supported by the EPSRC Grant No. EP/N509577/1. S.S. was supported by the EPSRC Grant No. EP/L016478/1. P.D.C. was supported by the NIHR Professorship RP 2014-04-046. A.O. was supported by the EPSRC Grants No. EP/P023231/1 and No. EP/M028100/1. M.E. was supported by the Royal

Academy of Engineering under the RA Eng Research Fellowship scheme. R.C.C. acknowledges funding from GlaxoSmithKline (GSK) under a collaborative framework agreement.

-
- [1] S. Wilkins, Y. I. Nesterets, T. Gureyev, S. Mayo, A. Pogany, and A. Stevenson, On the evolution and relative merits of hard X-ray phase-contrast imaging methods, *Phil. Trans. R. Soc. A* **372**, 20130021 (2014).
 - [2] A. Olivo and E. Castelli, X-ray phase contrast imaging: From synchrotrons to conventional sources, *Riv. Nuovo Cimento* **37**, 467 (2014).
 - [3] L. Rigon, X-ray imaging with coherent sources, *Compr. Biomed. Phys.* **2**, 193 (2014).
 - [4] A. Bravin, P. Coan, and P. Suortti, X-ray phase-contrast imaging: From pre-clinical applications towards clinics, *Phys. Med. Biol.* **58**, R1 (2012).
 - [5] S. Wilkins, T. E. Gureyev, D. Gao, A. Pogany, and A. Stevenson, Phase-contrast imaging using polychromatic hard X-rays, *Nature* **384**, 335 (1996).
 - [6] V. Cosslett and W. Nixon, X-ray shadow microscope, *Nature* **168**, 24 (1951).
 - [7] S. Mayo, T. Davis, T. Gureyev, P. Miller, D. Paganin, A. Pogany, A. Stevenson, and S. Wilkins, X-ray phase-contrast microscopy and microtomography, *Opt. Express* **11**, 2289 (2003).
 - [8] C. Fella, A. Balles, S. Zabler, R. Hanke, R. Tjeung, S. Nguyen, and D. Pelliccia, Laboratory x-ray microscopy on high brilliance sources equipped with wave guides, *J. Appl. Phys.* **118**, 034904 (2015).
 - [9] K. M. Sowa, B. R. Jany, and P. Korecki, Multipoint-projection X-ray microscopy, *Optica* **5**, 577 (2018).
 - [10] R. Grndl, M. Dierolf, L. Hehn, B. Günther, A. Ö. Yildirim, B. Gleich, K. Achterhold, F. Pfeiffer, and K. S. Morgan, Propagation-based phase-contrast X-ray imaging at a compact light source, *Sci. Rep.* **7**, 4908 (2017).
 - [11] M. Töpperwien, R. Grndl, D. Keppeler, M. Vassholz, A. Meyer, R. Hessler, K. Achterhold, B. Gleich, M. Dierolf, F. Pfeiffer *et al.*, Propagation-based phase-contrast X-ray tomography of cochlea using a compact synchrotron source, *Sci. Rep.* **8**, 4922 (2018).
 - [12] T. Tuohimaa, M. Otendal, and H. M. Hertz, Phase-contrast X-ray imaging with a liquid-metal-jet-anode microfocus source, *Appl. Phys. Lett.* **91**, 074104 (2007).
 - [13] M. Krenkel, M. Töpperwien, C. Dullin, F. Alves, and T. Salditt, Propagation-based phase-contrast tomography for high-resolution lung imaging with laboratory sources, *AIP Adv.* **6**, 035007 (2016).
 - [14] F. A. Vittoria, M. Endrizzi, G. K. Kallon, C. K. Hagen, F. Iacoviello, P. De Coppi, and A. Olivo, Multimodal phase-based X-ray microtomography with nonmicrofocal laboratory sources, *Phys. Rev. Appl.* **8**, 064009 (2017).
 - [15] G. Kallon, P. Diemoz, F. Vittoria, D. Basta, M. Endrizzi, and A. Olivo, Comparing signal intensity and refraction sensitivity of double and single mask edge illumination lab-based X-ray phase contrast imaging set-ups, *J. Phys. D: Appl. Phys.* **50**, 415401 (2017).

- [16] P. R. Munro, K. Ignatyev, R. D. Speller, and A. Olivo, The relationship between wave and geometrical optics models of coded aperture type X-ray phase contrast imaging systems, *Opt. Express* **18**, 4103 (2010).
- [17] A. Peterzol, A. Olivo, L. Rigon, S. Pani, and D. Dreossi, The effects of the imaging system on the validity limits of the ray-optical approach to phase contrast imaging, *Med. Phys.* **32**, 3617 (2005).
- [18] F. Arfelli, M. Assante, V. Bonvicini, A. Bravin, G. Cantatore, E. Castelli, L. Dalla Palma, M. Di Michiel, R. Longo, A. Olivo *et al.*, Low-dose phase contrast X-ray medical imaging, *Phys. Med. Biol.* **43**, 2845 (1998).
- [19] A. Olivo, Towards the exploitation of phase effects in clinical synchrotron radiation radiology, *Nucl. Instrum. Methods Phys. Res., Sect. A* **548**, 194 (2005).
- [20] T. E. Gureyev, Y. I. Nesterets, A. W. Stevenson, P. R. Miller, A. Pogany, and S. W. Wilkins, Some simple rules for contrast, signal-to-noise and resolution in in-line X-ray phase-contrast imaging, *Opt. Express* **16**, 3223 (2008).
- [21] D. Paganin, S. Mayo, T. E. Gureyev, P. R. Miller, and S. W. Wilkins, Simultaneous phase and amplitude extraction from a single defocused image of a homogeneous object, *J. Microsc.* **206**, 33 (2002).
- [22] A. Burvall, U. Lundström, P. A. Takman, D. H. Larsson, and H. M. Hertz, Phase retrieval in X-ray phase-contrast imaging suitable for tomography, *Opt. Express* **19**, 10359 (2011).
- [23] L. Brombal, B. Golosio, F. Arfelli, D. Bonazza, A. Contillo, P. Delogu, S. Donato, G. Mettivier, P. Oliva, L. Rigon, A. Taibi, G. Tromba, F. Zanconati, and R. Longo, Monochromatic breast computed tomography with synchrotron radiation: Phase-contrast and phase-retrieved image comparison and full-volume reconstruction, *J. Med. Imaging* **6**, 1 (2018).
- [24] T. E. Gureyev, Y. I. Nesterets, A. Kozlov, D. M. Paganin, and H. M. Quiney, On the unreasonable effectiveness of transport of intensity imaging and optical deconvolution, *JOSA A* **34**, 2251 (2017).
- [25] M. J. Kitchen, G. A. Buckley, T. E. Gureyev, M. J. Wallace, N. Andres-Thio, K. Uesugi, N. Yagi, and S. B. Hooper, CT dose reduction factors in the thousands using X-ray phase contrast, *Sci. Rep.* **7**, 15953 (2017).
- [26] Y. I. Nesterets and T. E. Gureyev, Noise propagation in X-ray phase-contrast imaging and computed tomography, *J. Phys. D: Appl. Phys.* **47**, 105402 (2014).
- [27] L. Brombal, S. Donato, D. Dreossi, F. Arfelli, D. Bonazza, A. Contillo, P. Delogu, V. Di-Trapani, B. Golosio, G. Mettivier *et al.*, Phase-contrast breast CT: The effect of propagation distance, *Phys. Med. Biol.* **63**, 24NT03 (2018).
- [28] M. Beltran, D. Paganin, K. Uesugi, and M. Kitchen, 2D and 3D X-ray phase retrieval of multi-material objects using a single defocus distance, *Opt. Express* **18**, 6423 (2010).
- [29] A. Zamir, P. C. Diemoz, F. A. Vittoria, C. K. Hagen, M. Endrizzi, and A. Olivo, Edge illumination X-ray phase tomography of multi-material samples using a single-image phase retrieval algorithm, *Opt. Express* **25**, 11984 (2017).
- [30] K. Shimizu and K. Omote, Multilayer optics for X-ray analysis, *Rigaku J.* **24** (2008).
- [31] P. Oberta, Y. Platonov, and U. Flechsig, Investigation of multilayer X-ray optics for the 6 keV to 20 keV energy range, *J. Synchrotron Radiat.* **19**, 675 (2012).
- [32] E. Samei, M. J. Flynn, and D. A. Reimann, A method for measuring the presampled MTF of digital radiographic systems using an edge test device, *Med. Phys.* **25**, 102 (1998).
- [33] http://henke.lbl.gov/optical_constants
- [34] G. Totonelli, P. Maghsoudlou, F. Georgiades, M. Garriboli, K. Koshy, M. Turmaine, M. Ashworth, N. J. Sebire, A. Pierro, S. Eaton *et al.*, Detergent enzymatic treatment for the development of a natural acellular matrix for oesophageal regeneration, *Pediatr. Surg. Int.* **29**, 87 (2013).
- [35] C. K. Hagen, P. Maghsoudlou, G. Totonelli, P. C. Diemoz, M. Endrizzi, L. Rigon, R.-H. Menk, F. Arfelli, D. Dreossi, E. Brun *et al.*, High contrast microstructural visualization of natural acellular matrices by means of phase-based X-ray tomography, *Sci. Rep.* **5**, 18156 (2015).
- [36] C. J. Scotton, B. Hayes, R. Alexander, A. Datta, E. J. Forty, P. F. Mercer, A. Blanchard, and R. C. Chambers, *Ex vivo* μ CT analysis of bleomycin-induced lung fibrosis for pre-clinical drug evaluation, *Eur. Respir. J.* **5**, erj01824 (2013).
- [37] V. Van Nieuwenhove, J. De Beenhouwer, F. De Carlo, L. Mancini, F. Marone, and J. Sijbers, Dynamic intensity normalization using eigen flat fields in X-ray imaging, *Opt. Express* **23**, 27975 (2015).
- [38] F. Brun, S. Pacilè, A. Accardo, G. Kourousias, D. Dreossi, L. Mancini, G. Tromba, and R. Pugliese, Enhanced and flexible software tools for X-ray computed tomography at the Italian synchrotron radiation facility Elettra, *Fundam. Inform.* **141**, 233 (2015).